INTERNATIONAL JOURNAL FOR NUMERICAL METHODS IN FLUIDS
Int. J. Numer. Meth. Fluids 2010; **62**:1232–1263

Two-dimensional prediction of time dependent, turbulent flow around a square cylinder confined in a channel

M. Raisee[1,*,†], A. Jafari[1], H. Babaei[1] and H. Iacovides[2]

[1]*Department of Mechanical Engineering, University of Tehran, P.O. Box 11365/4563, Tehran, Iran*
[2]*School of Mechanical, Aerospace and Civil Engineering, University of Manchester, Manchester, U.K.*

SUMMARY

This paper presents two-dimensional and unsteady RANS computations of time dependent, periodic, turbulent flow around a square block. Two turbulence models are used: the Launder–Sharma low-Reynolds number k–ε model and a non-linear extension sensitive to the anisotropy of turbulence. The Reynolds number based on the free stream velocity and obstacle side is $Re=2.2\times 10^4$. The present numerical results have been obtained using a finite volume code that solves the governing equations in a vertical plane, located at the lateral mid-point of the channel. The pressure field is obtained with the SIMPLE algorithm. A bounded version of the third-order QUICK scheme is used for the convective terms. Comparisons of the numerical results with the experimental data indicate that a preliminary steady solution of the governing equations using the linear k–ε does not lead to correct flow field predictions in the wake region downstream of the square cylinder. Consequently, the time derivatives of dependent variables are included in the transport equations and are discretized using the second-order Crank–Nicolson scheme. The unsteady computations using the linear and non-linear k–ε models significantly improve the velocity field predictions. However, the linear k–ε shows a number of predictive deficiencies, even in unsteady flow computations, especially in the prediction of the turbulence field. The introduction of a non-linear k–ε model brings the two-dimensional unsteady predictions of the time-averaged velocity and turbulence fields and also the predicted values of the global parameters such as the Strouhal number and the drag coefficient to close agreement with the data. Copyright © 2009 John Wiley & Sons, Ltd.

Received 15 November 2008; Revised 19 March 2009; Accepted 20 March 2009

KEY WORDS: vortex shedding; square cylinder; turbulence modeling; eddy-viscosity model

1. INTRODUCTION

Turbulent flow around bluff bodies has been attracting increasing attention not only because of its academic attractiveness, but also due to the relevant practical concerns associated with energy conservation and structural design. For instance, fuel consumption of aircrafts and vehicles can be decreased by reducing the aerodynamic drag and multi-story buildings and towers should

---

[*] Correspondence to: M. Raisee, Department of Mechanical Engineering, University of Tehran, P.O. Box 11365/4563, Tehran, Iran.
[†] E-mail: mraisee@ut.ac.ir

be designed in a way that avoids potentially disastrous wind-induced oscillations. Flow around a rectangular (or square) cylinder, confined in a channel, or subjected to the free-stream flow, is a basic geometry for studying flow around bluff body configurations. In such flows, various complex physical phenomena, including flow separation, reattachment, recirculation, and vortex shedding occur. Consequently, the interaction of these features produces a very challenging flow for experimentalists as well as CFD practitioners.

Over the last three decades, numerous experimental and numerical studies have been conducted to advance our understanding of different physical processes occurring in flow past a square cylinder. In these studies, the principal objective has mostly been to measure and/or to calculate the field variables and the related quantities from which to determine the drag and lift coefficients, as well as Strouhal and Nusselt numbers, the latter in cases where heat transfer also takes place. Some of these studies are reviewed here.

A number of investigations examined the effect of the angle of approach on the characteristics of flow around an obstacle. One of the earliest works is that reported by Lee [1] who conducted an experimental study to measure mean and fluctuating pressure fields for flow around a square cylinder in both uniform and turbulent flows at a Reynolds number of 1.8×10^5. Lee observed that when the cylinder was rotated with respect to the main stream direction, the vortex formation region moved downstream causing the drag to decrease. A minimum value of the drag coefficient was reached at an angle of incidence of about 15°. Further rotation of the cylinder produced a gradual increase in the drag coefficient as the vortex formation region moved upstream after the flow had reattached to the side wall. Lee also observed that the Strouhal number increased to a maximum at the angle at which the mean drag reached its minimum level. Later, Knisely [2] experimentally determined Strouhal numbers for a family of rectangular cylinders with aspect ratios ranging from 0.04 to 1 and flow angles of approach from 0° to 90°. Measurements were conducted in both a water channel with Reynolds numbers between 7.2×10^2 and 3.1×10^4 and in a wind tunnel with Reynolds numbers between 8.8×10^3 and 8.1×10^4. They found qualitatively similar behavior for Strouhal number with changing angle of approach for all aspect ratios examined, except for the lowest (thinnest plate). Norberg [3] studied the flow around rectangular cylinders and measured pressure forces at the angles of approach from 0° to 90°. In this investigation the Reynolds number was varied from 4.0×10^2 to 3.0×10^4. The results of this investigation showed a large influence of flow angle of approach on the flow structure due to reattachment and shear layer/edge interactions.

The effects of obstacle aspect ratio have been the topic of a number of experimental studies. Bearman and Trueman [4] conducted flow visualization studies of turbulent flow around rectangular cylinders for Reynolds numbers between $Re=2.0\times10^4$ and $Re=7.0\times10^4$ and presented detailed measurements for pressure, mean drag force, and shedding frequency. Among the rectangular cylinders examined, the maximum value of the drag coefficient occurred for a rectangular cylinder with an aspect ratio of 0.62. One of the most extensive experimental attempts to map out the flow characteristics around the rectangular cylinders was presented by Okajima *et al.* [5]. They determined Strouhal numbers for flow around rectangular cylinders with aspect ratios of 1–4 and Reynolds numbers between 7.0×10^1 and 2.0×10^4. For rectangular cylinders (aspect ratios of 2 and 3), they found a range of critical Reynolds numbers where flow patterns abruptly change with a sudden discontinuity in Strouhal number. The general tendency is a rapid rise in the Strouhal number, which occurs at relatively small angles of approach. The authors argued that the rapid rise is associated with reattachment of the separated shear layer. Lyn and Rodi [6] and Lyn *et al.* [7], using LDV, measured velocity components and turbulence quantities for turbulent flow around a square cylinder at $Re=2.2\times10^4$. Phase (ensemble)-averaged velocity and turbulence intensities

DOI: 10.1002/fld

were presented in various locations along the top surface of the obstacle as well as within the wake region downstream of the obstacle.

On the whole, it can be concluded that unsteady flow around rectangular cylinders is a very complex flow. On account of this complexity, the experimental data may be used in the CFD code validation to examine not only the capabilities of numerical schemes, but also to investigate the performance of the turbulence models. In recent years, unsteady flow around square cylinders has been the subject of several numerical investigations. One of the first numerical attempts to model the unsteady flow around an obstacle at low-Reynolds numbers was reported by Fromm and Harlow [8]. They studied the development of the vortex street behind a plate which has impulsively accelerated to a constant speed in a channel of finite width. In their study, the Reynolds number ranged between $Re=1.5\times10^1$ and $Re=6.0\times10^3$; however, only a few results were presented in their paper. Davis *et al.* [9] numerically investigated the effects of channel walls on flow around a square cylinder confined in a channel. They concluded that the presence of walls can significantly change the flow characteristics and increases both the drag coefficient and Strouhal number. Tamura and Kuwahara [10] numerically investigated the aerodynamics behavior of flow around a cylinder placed in a uniform stream at high-Reynolds numbers. They obtained numerical solutions for unsteady flow for various test cases by employing the 2-D and 3-D incompressible Navier–Stokes equations in a generalized coordinate system. No turbulence models were employed in their computations and the convective terms were approximated using the upwind scheme. They found that the flow patterns obtained by 2-D predictions had significant differences from those returned by the 3-D computations. Moreover, the computational results revealed that 3-D flow structures decrease both the drag coefficient and the lift amplitude. Hence, the authors concluded that the 3-D computational results are closer to the experimental data than the 2-D results. Kawamura and Kawashima [11], using a low-Reynolds number k–ε model, examined unsteady turbulent flow around a square cylinder confined in a channel. They compared their numerical results at $Re=2.2\times10^4$ with the experimental data of Lyn *et al.* [7]. The calculated turbulence levels behind the cylinder were significantly lower than those of the experimental data. However, the predicted Strouhal number and drag coefficient and also the phase-averaged velocity profiles were in satisfactory agreement with the measured data. Sohankar *et al.* [12] numerically studied flow around a square obstacle at a range of Reynolds number between $Re=4.5\times10^1$ and $Re=2.5\times10^2$. They found that the results strongly depended on the time step, computational grid, cell size, domain size, and blockage ratio. Decreasing the time step from 0.025 to 0.02 gave an increase of 1.5% in the root-mean square (RMS) lift, but with a time step of 0.05 the RMS lift decreased by 11.5%. Decreasing the size of the cell near the wall from 0.004 to 0.001 did not change the results significantly. When increasing the x_u/D (extent of domain upstream of the square cylinder) from 7.5 to 11.1 the RMS lift decreased by 9.3%. A further increase up to $x_u/D=18.3$ resulted in negligible changes. Richmond-Bryant [13] presented a numerical work providing a verification study of Reynolds-averaged Navier–Stokes (RANS) methods for the problem of airflow past a circular cylinder at $Re=5232$. She examined the standard and renormalized group (RNG) versions of the k–ε model, along with the Boussinesq [14] and Craft *et al.* [15] stress strain-rate relation. Verification testing with the standard and RNG k–ε models suggested that the simulations exhibited global monotonic convergence for the Boussinesq models. However, the global order of accuracy of the methods was much lower than the expected order of accuracy of two. Poor iterative and global grid convergence was found for the RNG k–ε model with Craft *et al.* [15] stress strain-rate relation.

Bosch and Rodi [16] utilized the standard and Kato and Launder [17] modified high-Reynolds number two-equation k–ε models to numerically solve the turbulent flow around a square cylinder at Reynolds number of 22 000 and compared their predictions with experimental data of Lyn *et al.* [7]. It should be noted that the main feature of the Kato–Launder k–ε is an *ad hoc* modification to the generation rate term of the turbulent kinetic energy, which, compensating for the known weakness of the effective-viscosity approximation, reduces the generation rate at the stagnation point region. To resolve the viscous effected near-wall regions, they employed the wall-function approach and the one-equation turbulence model. The results of their calculations showed that the Kato–Launder model produced better predictions for the drag and lift coefficients and Strouhal number in comparison with those of the standard model. Younis and Przulj [18] compared the results of the RNG, standard and one modified k–ε models with experimental results in vortex shedding around a square and circular cylinders. They also employed the one-equation model in near-wall regions. They found that the modified model produces results that are in close agreement with the measurements, especially for the RMS values of the drag and lift coefficients. The RNG model underestimates the mean and RMS values of the drag coefficient, as well as the length of the recirculation zone. Saha *et al.* [19] also studied the turbulent unsteady wake behind a square cylinder with the standard, Kato–Launder, and RNG k–ε models. By comparing the time-averaged velocities at some locations and the kinetic energy of the fluctuations that were obtained by using these models, they showed that the best predictions are those of the Kato–Launder model. Some studies also used the large eddy simulation (LES) as well as RANS to obtain the turbulent vortex-shedding flow around a square cylinder. For example, Rodi [20] presented a comparison of RANS and LES calculations of the flow around bluff bodies—a 2D square cylinder at $Re=22000$ and a surface mounted cube at $Re=40\,000$. He reported results from RANS calculations obtained with various versions of the k–ε model and LES ones presented in a workshop. From the comparisons he concluded that in all RANS calculations, the turbulence fluctuations are severely underpredicted. However, the Kato–Launder modification combined with the two-layer approach improved the results. In general, LES seemed to give a better representation of the details of the flow.

The preceding numerical studies appear to suggest that when it comes to the application of 2-D unsteady RANS (URANS) the variants of the effective-viscosity k–ε tested have been shown to be only partially successful in predicting the measured time-averaged features of unsteady flows behind square cylinders. The most successful variant, the Kato–Launder, is one that tries in an *ad hoc* way to compensate for one of the weaknesses of the effective-viscosity approach. These comparisons inevitably suggest that the turbulence models that account for the effects of turbulence anisotropy in a manner more rigorous than the Kato–Launder variant need to be tested in 2-D URANS computations of such flows.

The objective of this study is to further pursue the two-dimensional unsteady RANS approach, as the route to the prediction of these oscillatory wake flows, because of the computational savings it offers in comparison with LES, or even three-dimensional URANS. Two turbulence models are tested, both of which are low-Reynolds number models. The Launder–Sharma [21] linear k–ε is first tested, which has been in use for several decades and has been applied to the computation of a variety of flows. Then in order to be able to take into account the effects of the anisotropy of the turbulence field, a non-linear version of the k–ε model, due to Craft *et al.* [22] have also been employed. In the latter, the elements of the Reynolds stress tensor are obtained from algebraic expressions, which are cubic in terms of the strain-rate tensor and as a result of which the anisotropy of the turbulence is more faithfully reproduced. Our earlier research effort (Raisee *et al.* [23, 24] and Craft *et al.* [25] show that this model has a good track record in predicting complex and unsteady flows.

DOI: 10.1002/fld

2. PROBLEM DESCRIPTION

Figure 1 shows the geometry of the flow investigated in this study. The computational domain consists of a square cylinder of length-side D and blockage ratio $(\beta = D/H)$ of 0.07, which is located in the middle of the channel. In the relevant experimental work of Lyn *et al.* [7], the channel height was chosen as $H = 14D$ to remove the effects of channel walls on the flow field. Also, the channel side along the lateral direction was long. Thus, the three-dimensional effects due to side walls may be ignored and computations may be performed in two dimensions. The distances of the obstacle center from the inlet and outlet planes of the channel are set to $4.5D$ and $14D$, respectively. The Reynolds number based on inlet velocity (U_{in}) and obstacle side (D) is 2.2×10^4. The available experimental data for this geometry are time-averaged velocity and turbulence intensity profiles, which were measured using LDV.

3. GOVERNING EQUATIONS

For an unsteady, Newtonian, and incompressible flow, the conservation laws of mass and momentum obtained with the ensemble averaging are written as:

Continuity:

$$\frac{\partial U_j}{\partial x_j} = 0 \tag{1}$$

Momentum:

$$\frac{\partial U_i}{\partial t} + \frac{\partial (U_i U_j)}{\partial x_j} = -\frac{1}{\rho}\frac{\partial P}{\partial x_i} + \frac{\partial}{\partial x_j}\left(\nu \frac{\partial U_i}{\partial x_j} - \overline{u_i u_j}\right) \tag{2}$$

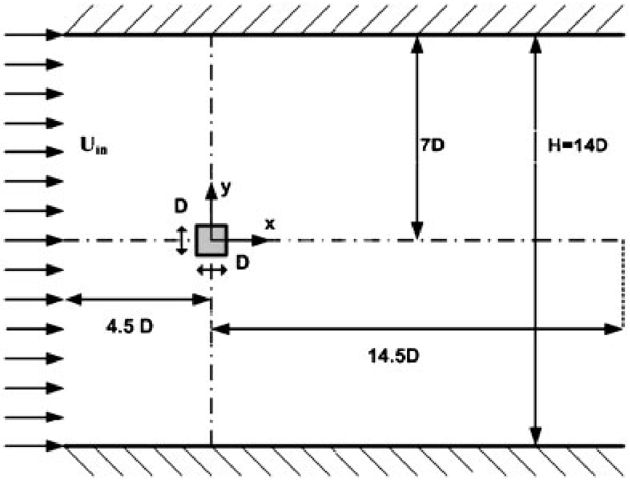

Figure 1. Flow configuration investigated ($\beta = 7\%$ and $Re = 2.2 \times 10^4$).

where P is the pressure, U_i denotes the mean velocity vector, and $\overline{u_i u_j}$ are the unknown Reynolds stress tensor.

4. TURBULENCE MODELING

The turbulence models employed for computations are the low-*Re* Launder and Sharma [21] k–ε model, and a modified version of non-linear low-*Re* k–ε model [22].

4.1. Linear low-Re k–ε model, Launder and Sharma [21]

This model is an extension of high-Reynolds k–ε model that accounts for the wall damping of turbulence and hence can be used across the viscous sublayer. In this turbulence model, the Reynolds stresses are obtained via the Boussinesq hypothesis [14], shown below, which result in largely isotropic normal stresses, since $|v_t(\partial U/\partial x)| = |v_t(\partial V/\partial y)| \ll \frac{2}{3}k$.

$$\overline{u_i u_j} = \frac{2}{3}k\delta_{ij} - v_t\left(\frac{\partial U_i}{\partial x_j} + \frac{\partial U_j}{\partial x_i}\right) \tag{3}$$

where k is the turbulent kinetic energy.

The turbulent viscosity is obtained from the following equation:

$$v_t = C_\mu f_\mu \frac{k^2}{\tilde{\varepsilon}} \tag{4}$$

where C_μ coefficient is given in Table I and $\tilde{\varepsilon}$ is the dissipation rate of turbulent kinetic energy.

The distributions of turbulent kinetic energy (k) and homogeneous dissipation rate ($\tilde{\varepsilon}$) are obtained by solving the following transport equations:

$$\frac{Dk}{Dt} = \frac{\partial}{\partial x_j}\left[\left(v + \frac{v_t}{\sigma_k}\right)\frac{\partial k}{\partial x_j}\right] + P_k - \tilde{\varepsilon} - 2v\left(\frac{\partial\sqrt{k}}{\partial x_j}\right)^2 \tag{5}$$

$$\frac{D\tilde{\varepsilon}}{Dt} = \frac{\partial}{\partial x_j}\left[\left(v + \frac{v_t}{\sigma_\varepsilon}\right)\frac{\partial\tilde{\varepsilon}}{\partial x_j}\right] + f_1 c_{\varepsilon 1}\frac{\tilde{\varepsilon}}{k}P_k - f_2 c_{\varepsilon 2}\frac{\tilde{\varepsilon}^2}{k} + E + S_\varepsilon \tag{6}$$

where variable $\tilde{\varepsilon}$ can be related to the real dissipation rate, ε, through:

$$\tilde{\varepsilon} = \varepsilon - 2v\left[\frac{\partial\sqrt{k}}{\partial x_j}\right]^2 \tag{7}$$

Table I. Empirical constants for the linear low-Reynolds number k–ε model.

c_μ	$c_{\varepsilon 1}$	$c_{\varepsilon 2}$	σ_k	σ_ε	σ_θ
0.09	1.44	1.92	1.0	1.3	0.9

The turbulent kinetic energy production term, P_k, is given by:

$$P_k = -\overline{u_i u_j}\frac{\partial U_i}{\partial x_j} \tag{8}$$

The damping functions f_1, f_2, and f_μ have the following expressions:

$$f_1 = 1, \quad f_2 = 1 - 0.3\exp(-\tilde{R}_t^2), \quad f_\mu = \exp[-3.4/(1+0.02\tilde{R}_t)^2] \tag{9}$$

where $\tilde{R}_t = k^2/\nu\tilde{\varepsilon}$ is the local turbulent Reynolds number.

The constants in the turbulent kinetic energy and the dissipation rate equations are given in Table I.

The E term was first introduced by Jones and Launder [26] and is expressed as:

$$E = 2\nu\nu_t\left(\frac{\partial^2 U_i}{\partial x_j\,\partial x_i}\right)^2 \tag{10}$$

The extra source term, S_ε, stands for the 'Yap' correction term that is discussed in the later sections.

4.2. *Non-linear low-Re k–ε model, Craft et al.* [22]

In this turbulence model, turbulent stresses are obtained via the constitutive relation below, which is cubic in terms of the strain rate, and as result is able to return an anisotropic turbulence field.

$$\begin{aligned}\overline{u_i u_j} &= \frac{2}{3}k\delta_{ij} - \nu_t S_{ij} + c_1\frac{\nu_t k}{\tilde{\varepsilon}}\left(S_{ik}S_{kj} - \frac{1}{3}S_{kl}S_{kl}\delta_{ij}\right)\\ &\quad + c_2\frac{\nu_t k}{\tilde{\varepsilon}}(\Omega_{ik}S_{kj} + \Omega_{jk}S_{ki}) + c_3\frac{\nu_t k}{\tilde{\varepsilon}}\left(\Omega_{ik}\Omega_{jk} - \frac{1}{3}\Omega_{lk}\Omega_{lk}\delta_{ij}\right)\\ &\quad + c_4\frac{\nu_t k^2}{\tilde{\varepsilon}^2}(S_{ki}\Omega_{lj} + S_{kj}\Omega_{li})S_{kl} + c_5\frac{\nu_t k^2}{\tilde{\varepsilon}^2}\left(\Omega_{il}\Omega_{lm}S_{mj} + S_{il}\Omega_{lm}\Omega_{mj} - \frac{2}{3}S_{lm}\Omega_{mn}\Omega_{nl}\delta_{ij}\right)\\ &\quad + c_6\frac{\nu_t k^2}{\tilde{\varepsilon}^2}S_{ij}S_{kl}S_{kl} + c_7\frac{\nu_t k^2}{\tilde{\varepsilon}^2}S_{ij}\Omega_{kl}\Omega_{kl}\end{aligned} \tag{11}$$

where S_{ij} and Ω_{ij} are strain and vorticity rate tensors:

$$S_{ij} = \left(\frac{\partial U_i}{\partial x_j} + \frac{\partial U_j}{\partial x_i}\right), \quad \Omega_{ij} = \left(\frac{\partial U_i}{\partial x_j} - \frac{\partial U_j}{\partial x_i}\right) \tag{12}$$

The model coefficients, c_1–c_7, have been calibrated by Craft *et al.* [22], by reference to several flows, including homogeneous shear flows, swirling flows, and curved channel flows. The values of these coefficients are given in Table II.

The k and $\tilde{\varepsilon}$ transport equations and eddy-viscosity formulation are similar to those of linear model, however, for modeling of c_μ the following expression was proposed by Craft *et al.* [27].

$$c_\mu = \min\left[0.09, \frac{1.2}{1+3.5\eta+f_{RS}}\right] \tag{13}$$

Table II. Values of coefficients in the non-linear k–ε model.

c_1	c_2	c_3	c_4	c_5	c_6	c_7
-0.1	0.1	0.26	$-10c_\mu^2$	0	$-5c_\mu^2$	$5c_\mu^2$

with

$$\eta = \max(\tilde{S}, \tilde{\Omega}) \tag{14}$$

where the strain and vorticity invariants are expressed as:

$$\tilde{S} = \frac{k}{\tilde{\varepsilon}}\sqrt{0.5\,S_{ij}S_{ij}}, \quad \tilde{\Omega} = \frac{k}{\tilde{\varepsilon}}\sqrt{0.5\Omega_{ij}\Omega_{ij}} \tag{15}$$

and

$$f_{RS} = 0.235[\max(0, \eta - 3.333)]^2 \exp(-\tilde{R}_t/400) \tag{16}$$

The viscous damping function of v_t is provided by the function f_μ:

$$f_\mu = 1 - \exp\left\{ -\left(\frac{\tilde{R}_t}{90}\right)^{1/2} - \left(\frac{\tilde{R}_t}{400}\right)^2 \right\} \tag{17}$$

The near-wall source term E is now expressed as:

$$E = \begin{cases} 0.0022\dfrac{\tilde{S}v_t k^2}{\tilde{\varepsilon}}\left(\dfrac{\partial^2 U_i}{\partial x_j\, \partial x_k}\right)^2, & \tilde{R}_t \leqslant 250 \\ 0, & \tilde{R}_t > 250 \end{cases} \tag{18}$$

Length-scale correction term: It is well known that, as demonstrated by Yap [28], in separated flows, the Launder and Sharma version of $\tilde{\varepsilon}$-equation returns excessively high levels of near-wall turbulence. To address this problem, Yap [28] introduced an extra source term into the dissipation rate equation, 'Yap', based on the wall distance, y_w.

$$S_\varepsilon = \text{Yap} = 0.83\frac{\tilde{\varepsilon}^2}{k}\max[(\ell/\ell_e - 1)(\ell/\ell_e)^2, 0] \tag{19}$$

where ℓ is the turbulent length scale $k^{3/2}/\tilde{\varepsilon}$, the equilibrium length scale $\ell_e = 2.55y_w$, and y_w is the distance to the wall.

To eliminate the dependence of the above source term on the wall distance, a differential form of the length-scale correction was proposed by Iacovides and Raisee [29]

$$S_\varepsilon = [\text{NYP}] = \max[C_\omega F(F+1)^2\tilde{\varepsilon}^2/k, 0] \tag{20}$$

where

$$F = \{[(\partial\ell/\partial x_i)(\partial\ell/\partial x_i)]^{1/2} - (\mathrm{d}l_e/\mathrm{d}y)\}/c_l \tag{21}$$

represents the difference between the predicted length-scale gradient with $\ell = k^{3/2}/\tilde{\varepsilon}$ and the 'equilibrium length-scale gradient', $\mathrm{d}l_e/\mathrm{d}y$, defined by

$$\mathrm{d}l_e/\mathrm{d}y = c_l[1-\exp(-B_\varepsilon R_t)] + B_\varepsilon c_l R_t \exp(-B_\varepsilon R_t) \tag{22}$$

where $c_l = 2.55$, $B_\varepsilon = 0.1069$, and $C_\omega = 0.83$.

In order to reduce the amount of correction in the regions of high η, a modified version of the Iacovides and Raisee [29] differential correction term was proposed by Craft *et al.* [27], where the coefficient C_ω is taken as

$$C_\omega = \frac{0.83\min(1, \tilde{R}_t/5)}{[0.8+0.7(\eta'/3.33)^4\exp(-\tilde{R}_t/12.5)]} \tag{23}$$

where the quantity η' is defined in the same way as η but, to enhance stability, the Kolmogorov timescale is used as a lower limit on the timescale $k/\tilde{\varepsilon}$ employed in the expressions for $\tilde{S}$ and $\tilde{\Omega}$, in a manner similar to the proposal of Durbin [30]:

$$\tilde{S} = \max[k/\tilde{\varepsilon}, \sqrt{\nu/\varepsilon}]\sqrt{0.5 S_{ij}S_{ij}}, \quad \tilde{\Omega} = \max[k/\tilde{\varepsilon}, \sqrt{\nu/\varepsilon}]\sqrt{0.5\Omega_{ij}\Omega_{ij}} \tag{24}$$

The limited $\tilde{R}_t$-dependent damping is included for numerical stability.

5. NUMERICAL METHODS

The general form of the governing equations of mean flow and turbulence is written as

$$\underbrace{\frac{\partial}{\partial t}(\rho\phi)}_{\text{Unsteady}} + \underbrace{\frac{\partial}{\partial x}(\rho\phi U) + \frac{\partial}{\partial y}(\rho\phi V)}_{\text{Convection}} = \underbrace{\frac{\partial}{\partial x}\left(\Gamma_\phi \frac{\partial\phi}{\partial x}\right) + \frac{\partial}{\partial y}\left(\Gamma_\phi \frac{\partial\phi}{\partial y}\right)}_{\text{Diffusion}} + \underbrace{S_\phi}_{\text{Source}} \tag{25}$$

where x and y are the coordinates in the stream-wise and cross-stream directions, respectively, and ϕ represents the velocity component (U and V) and turbulence quantities (k and ε). Γ_ϕ is an effective diffusion coefficient and S_ϕ denotes the total source term in each transport equation.

In the present study, the governing equations are solved using the finite volume methodology in a semi-staggered grid system. In such a grid distribution, both velocity components (U and V) are computed and stored in the same nodal position and the velocity nodes are located at the corners of the scalar control volume. Thus, only two sets of control volumes are needed for the computations. The pressure field is linked to that of velocity through the well-known SIMPLE pressure-correction algorithm. To avoid stability problems associated with pressure–velocity decoupling, the Rhie and Chow [31] interpolation scheme is also employed. A bounded third-order QUICK differencing scheme, developed by Iacovides [32], is employed for the approximation of the convective terms in all transport equations.

In the QUICK scheme, depending on the flow direction, the value of unknown dependent variable ϕ at each face of control volume is evaluated from a quadratic polynomial that passes through

DOI: 10.1002/fld

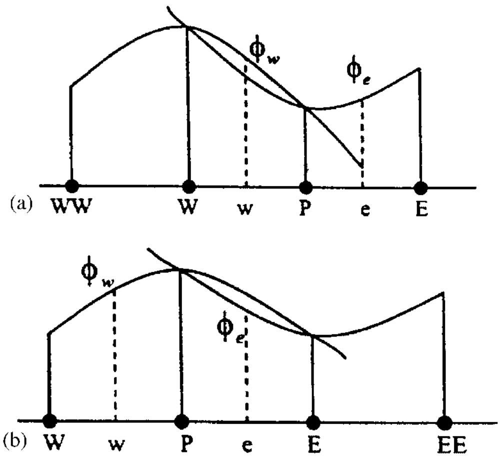

Figure 2. The QUICK scheme: (a) $F_e > 0$ and $F_w > 0$ and (b) $F_e < 0$ and $F_w < 0$.

a grid point downstream and two grid points upstream of each face. For example, as shown in Figure 2, the value of ϕ at the east face of control volume ϕ on a uniform grid is obtained by

$$\phi_e = \begin{cases} \phi_P + Q_e^+, & F_e > 0 \\ \phi_E + Q_e^-, & F_e < 0 \end{cases} \tag{26}$$

where ϕ_P and ϕ_E are the values of upwind approximation and QUICK scheme corrections Q_e^+ and Q_e^- are expressed as:

$$Q_e^+ = \tfrac{1}{8}[-\phi_W + 3\phi_E - 2\phi_P] \tag{27}$$

$$Q_e^- = \tfrac{1}{8}[-\phi_{EE} + 3\phi_P - 2\phi_E] \tag{28}$$

In the unsteady calculations, the time derivatives are approximated using the second-order Crank–Nicolson [33]. Obviously, the time step in the time-marching calculation of vortex-shedding flow is an important parameter. If a very large value is chosen, the global accuracy may be seriously affected. The predicted stream-wise velocity at six locations obtained from unsteady computation with the linear k–ε model for dimensionless time steps $\Delta t^* = H\,\Delta t/U_{\text{in}} = 0.002, 0.001$, and 0.0005 are shown in Figure 3. Within the wake region at $x/D = 1.0$ and $x/D = 1.5$, while some differences are observed between profiles obtained with $\Delta t^* = 0.002$ and 0.001, predictions with a smaller time step of $\Delta t^* = 0.0005$ do not significantly differ from those of $\Delta t^* = 0.001$. Moreover, with reference to the methodology discussed in Richmond-Bryant [13], global relative two-norm error for stream-wise velocity is calculated for 5000 points located in the region $-1 \leqslant x/D \leqslant 3$, $0 \leqslant y/D \leqslant 1$. The error resulting from increasing the time step from $\Delta t^* = 0.001$ to $\Delta t^* = 0.002$ is 6.03×10^{-4}, and from $\Delta t^* = 0.0005$ to $\Delta t^* = 0.001$ is 2.06×10^{-4}. Thus, the results presented here, which have been obtained with $\Delta t^* = 0.001$, are sufficiently accurate. The convergence ratio based on the global error norm is 0.34. This indicates that the time-step convergence is monotonic.

As shown in Figure 4, the grid used for computations consists of (105×102) grid nodes in the stream-wise (x) and cross-stream (y) directions, respectively. For this grid, the y^+ values for the

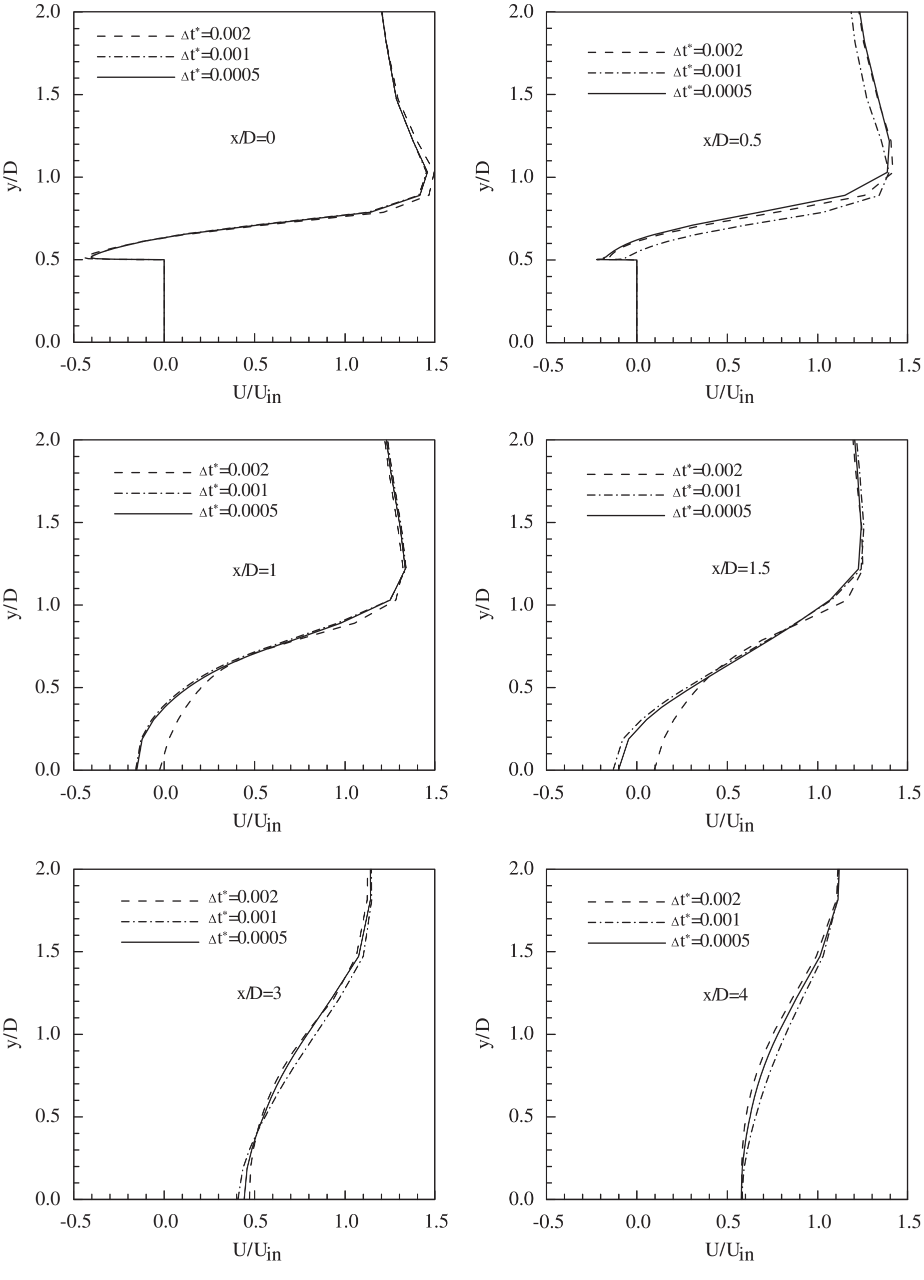

Figure 3. Comparison of stream-wise velocity profiles for various time steps.

near-wall nodes are less than unity. To assess the accuracy of the results presented in this paper, a series of grid-independence tests have been carried out using several grids for the linear k–ε model. In Figure 5, the stream-wise velocity profiles at six stream-wise locations for three different

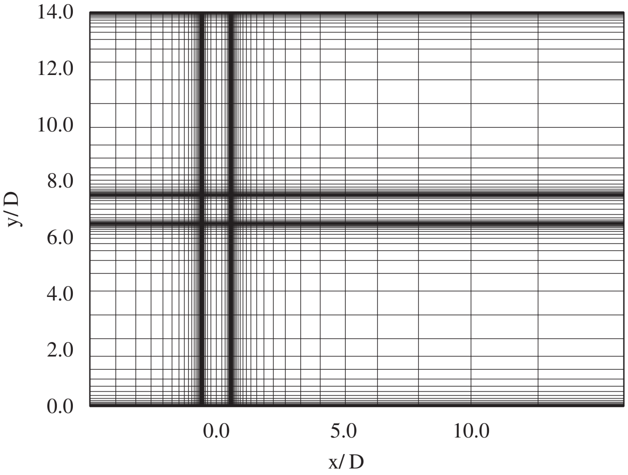

Figure 4. Computational grid with 105×102 nodes in the stream-wise and cross-stream directions ($\beta = 7\%$ and $Re = 2.2 \times 10^4$).

meshes including 105×102 (the main mesh utilized in this study), 85×82, and 145×138 are represented. While some differences are observed between results obtained with the 85×82 mesh and those of the 105×102, further grid refinement does not alter the velocity field predictions. In addition, global relative two-norm error resulting from changing the mesh from 105×102 to 85×82 is 3.87×10^{-3}, and from 145×138 to 105×102 is 1.63×10^{-3}. Thus, these results show that the grid used in the present study is sufficiently fine to produce accurate results. The convergence ratio based on the global error norm is 0.42. This indicates that the grid convergence is monotonic.

6. BOUNDARY CONDITIONS

No-slip boundary conditions are used at the solid walls. In accordance with the experiment of Lyn *et al.* [7], a uniform flow with bulk velocity U_{in} is assumed for the inlet of the channel. The inlet turbulent kinetic energy is set to $k_{\text{in}} = (0.02U_{\text{in}})^2$, while the dissipation is obtained from $\varepsilon_{\text{in}} = k_{\text{in}}^{3/2}/\ell$ where $\ell = 0.2D$. For this configuration, as indicated in a number of numerical studies such as Rodi [20], choosing $v_t/v = 10$ for the inlet flow leads to numerical results consistent with the experimental data. In the present study, an inlet lengthscale $\ell = 0.2D$ is chosen, which using the turbulent viscosity expression $v_t/v = C_\mu \ell k^{1/2}/v$ with $k_{\text{in}} = (0.02U_{\text{in}})^2$, $C_\mu = 0.09$, and $Re = U_{\text{in}}D/v = 22\,000$, results in a value of v_t/v of 7.92.

At the outlet boundary, a zero gradient boundary condition is used for k and ε. For U, a convective-type boundary condition of the form

$$\frac{\partial U}{\partial t} + U_{\text{in}} \frac{\partial U}{\partial x} = 0 \tag{29}$$

is used, while the cross-stream component (V) is set to zero.

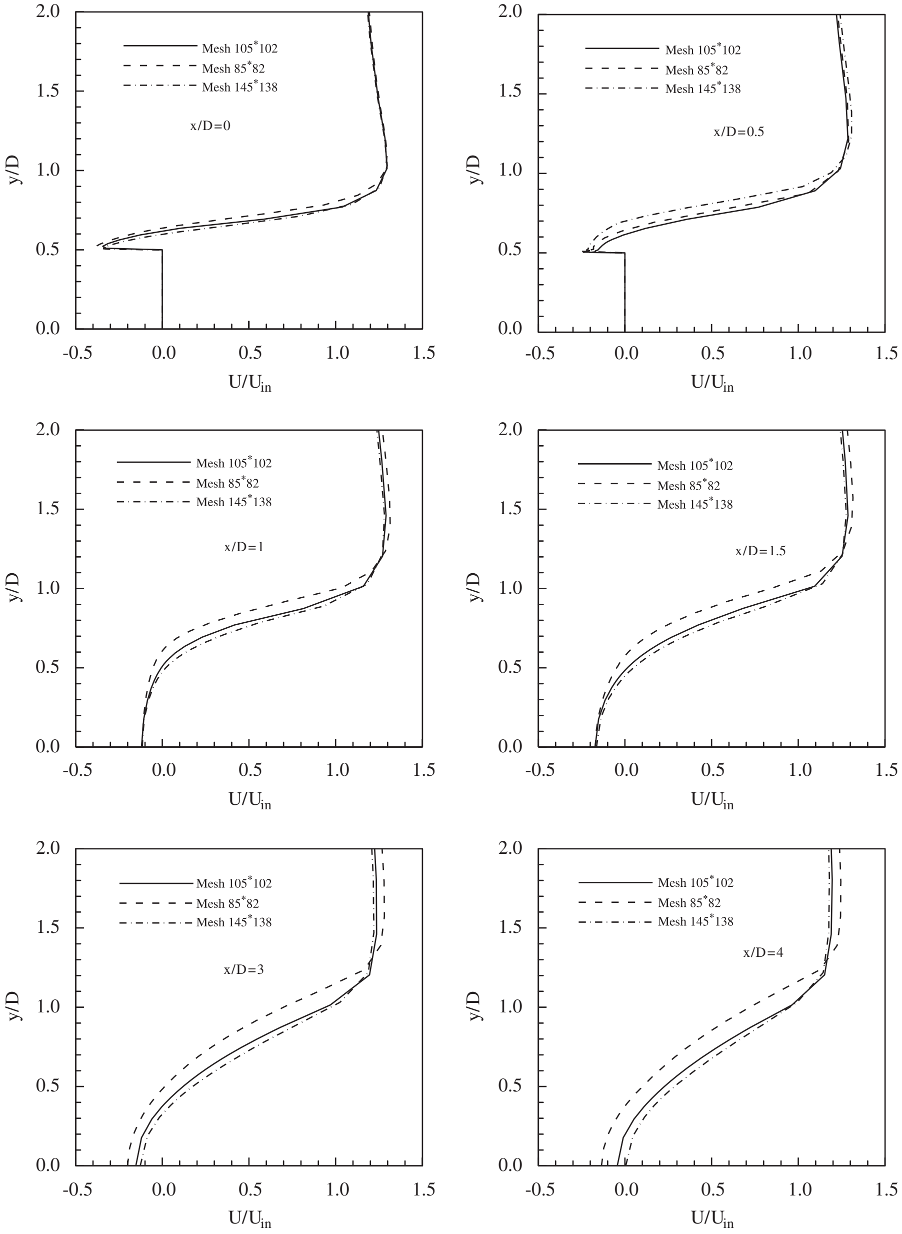

Figure 5. Comparison of stream-wise velocity profiles for various meshes.

Since there is a pressure drop along the channel, the output pressure is set equal to sum of the pressure of the upstream nodes and a uniform bulk pressure correction ppd. A uniform pressure difference, denoted as ppd below, is imposed across the exit plane, the value of which is determined iteratively, through the overall mass balance. More specifically, at each iteration, a correction to the exit plane pressure difference, denoted by pppd, is computed from the difference between the inlet and outlet flow rates as shown by the following equation:

$$\text{pppd} = \frac{\dot{m} - \int_A \rho U^{Ni-1} \mathrm{d}A}{\int_A \rho D U^{Ni-1} \mathrm{d}A} \tag{30}$$

where $\dot{m}$ represents the inlet mass flow rate.

This correction, is then under relaxed, using the factor urfp, and added to the overall exit-plane pressure difference, as shown in the following equation:

$$\text{ppd} = \text{ppd} - \text{urfp} \times \text{pppd} \tag{31}$$

When convergence is reached, pppd becomes zero and ppd remains unchanged and provides the difference between the pressure of the exit nodes (Ni) and that of the nodes at the upstream line (iN−1), as shown by the following equation:

$$P^{Ni} = P^{Ni-1} + \text{ppd} \tag{32}$$

The U-velocities at the upstream nodes (iN−1) are subsequently corrected, at each iteration, by the following relation:

$$U^{Ni-1} = U^{Ni-1} + DU^{Ni-1}\text{pppd} \tag{33}$$

7. RESULTS AND DISCUSSION

This section examines the effectiveness of the two low-*Re* k–ε models (described in Section 4) in reproducing characteristics of unsteady turbulent flow around a square obstacle. Here, the steady state results are also included as a set of baseline predictions. The predicted streamlines resulting from steady-state computations and using the linear and non-linear low-*Re* k–ε models are presented in Figure 6. The steady flow simulation shows that the flow separates at the leading edges of the cylinder forming two intense recirculation bubbles on the top and bottom surfaces of the obstacle. Downstream of the obstacle, a pair of large and symmetric counter rotating vortices is formed. Experimental evidence (e.g. [6, 7]) suggests that such behavior (steady and symmetric vortices) is not physically correct at high-Reynolds number flows. The length of the recirculation region obtained from the non-linear k–ε model calculation is shorter, but wider than that obtained using the linear k–ε model, which is more consistent with the experimental results.

In the present study, the steady solution is used as an initial condition for the unsteady computations.

The results of unsteady computations obtained using the linear and non-linear low-*Re* k–ε models (during one period of vortex shedding (τ)) are presented in Figures 7 and 8 in terms of streamlines ($-10000<\psi<10000$). The period of vortex shedding (τ) is obtained by calculating the time difference between two consecutive peaks in the time history of stream function in a point located in the unsteady wake region. It can be seen that at $t/\tau = \frac{1}{20}$ there is an anti-clockwise vortex in development at the lower base corner, being fed by the separation at that corner. As it grows, with increasing strength but being rather fixed in position, the reattachment point on the rear side is being pushed upwards. When the attachment point reaches the upper base corner at $t/\tau = \frac{7}{20}$, a new clock-wise vortex is about to be formed at that corner, which thereafter feeds its circulation.

DOI: 10.1002/fld

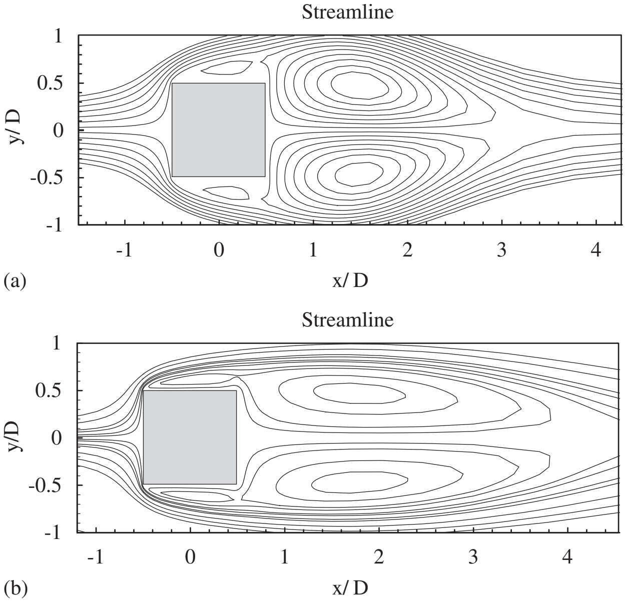

Figure 6. Streamline contours obtained from steady computations using: (a) non-linear k–ε model and (b) linear k–ε model ($\beta = 7\%$ and $Re = 2.2 \times 10^4$).

As this new vortex grows, the old vortex is being pushed away from the obstacle and is eventually shed to the wake. In general, the same trend occurs in the other periods. A comparison between the streamlines of the instantaneous flow field, predicted by the linear k–ε in Figure 7, and those of its non-linear counterpart of Figure 8, shows that while the two models predict a similar overall flapping motion, the linear k–ε predicts a more intense flow separation behind the block, which extends further downstream. These differences and their cause are discussed further in subsequent comparisons.

In Figure 9, the steady U-velocity predictions of the linear k–ε model and unsteady computations of time-averaged U-velocity with both linear and non-linear k–ε models are presented and compared with the experimental data of Lyn *et al.* [7]. It should be mentioned that since the actual flow is unsteady, the statistical values are obtained by post-processing of the measured instantaneous velocity field. The time-averaged profiles obtained via time-averaging process over one period are directly comparable with the measured counterparts.

From the six stations shown in Figure 9, two locations ($x/D = 0.0$ and 0.5) are chosen to be on top of the obstacle, two locations ($x/D = 1.0$ and 1.5) are within the recirculation region to study the flow behavior in the unsteady wake region and the remaining two stations ($x/D = 3.0$ and 4.0) are in the recovery region to see how well the turbulence models perform in this region.

Over the top surface of the obstacle at $x/D = 0.0$ and $x/D = 0.5$, and also at the first station within the wake, i.e. $x/D = 1.0$, there are only small differences between the steady and unsteady flow predictions of the time-averaged U-velocity, though the results returned from the unsteady predictions are generally in better agreement with the experimental data. At the second station within the wake, i.e. at $x/D = 1.5$, the differences between the steady and unsteady predictions now

DOI: 10.1002/fld

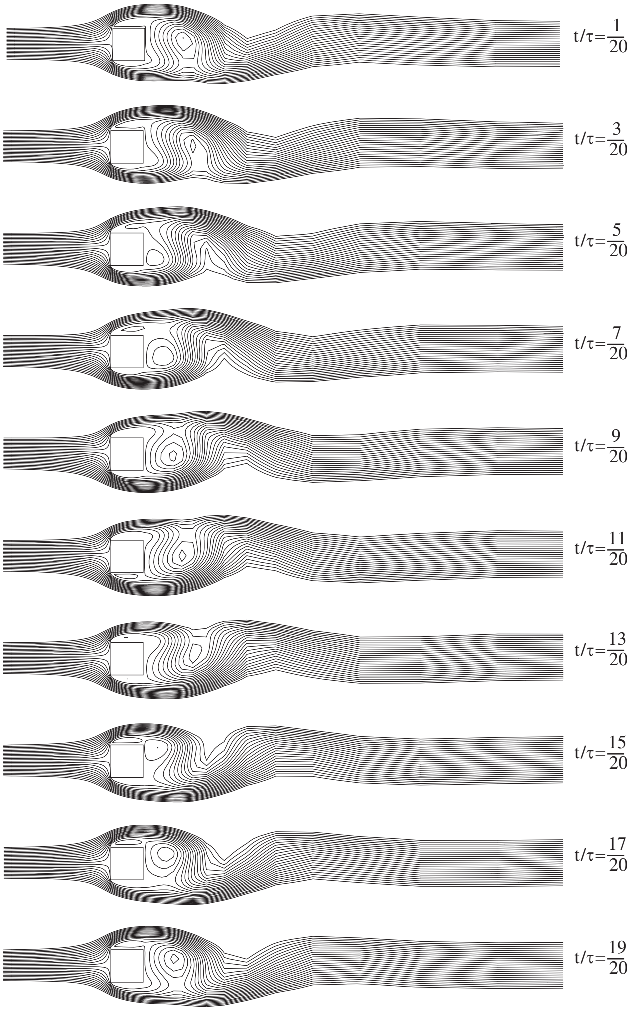

Figure 7. Predicted stream lines of instantaneous flow field at one period and at 10 different times using the linear k–ε model ($\beta = 7\%$ and $Re = 2.2 \times 10^4$).

become larger and, while the steady computations fail to capture the experimental data, the time-averaged velocity profile obtained with the unsteady flow simulation is in reasonable agreement with the experimental data. Further downstream at $x/D = 3.0$ and 4.0, there are significant differences in predicted time-averaged U-velocity profiles with steady and unsteady computations. As can be clearly seen, in the unsteady flow simulations, the additional flow mixing, which results from the vortex shedding behind the block, leads to a faster recovery in the wake flow. This significantly improves the predictions of the time-averaged velocity field, bringing the numerical results obtained from the unsteady computations to close agreement with the measurements. It is noted that the non-linear k–ε model, in closer accord with the measurements, returning a faster recovery of the wake region downstream of the obstacle, a feature consistent with the comparisons of the predicted

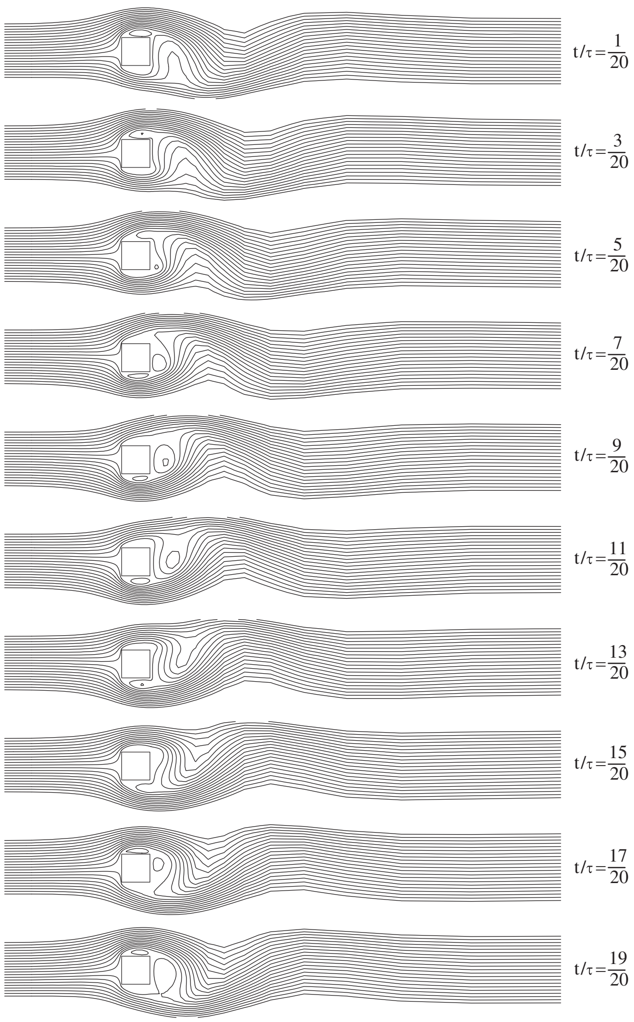

Figure 8. Predicted stream lines of instantaneous flow field at one period and at 10 different times using the non-linear k–ε ($\beta = 7\%$ and $Re = 2.2 \times 10^4$) model.

flow streamlines of the instantaneous flow field of Figures 7 and 8 and implies that the non-linear model predicts a stronger mixing of the flow downstream of the square cylinder.

In Figure 10, the steady and unsteady flow predictions of time-averaged cross-stream velocity at several locations are compared with the experimental data of Lyn *et al.* [7]. As also seen in the previous figure, here again at the first station, i.e. $x/D = 0.0$, there is little difference between the steady and unsteady flow predictions, though some evidence of improvement in predictions is visible in the unsteady flow computations. At the second station, i.e. at $x/D = 0.5$, while the steady flow computation severely under predicts the V-velocity, the unsteady flow solutions substantially improve the predictions. Immediately after the block, $x/D = 1.0$ and 1.5, where the vortex shedding

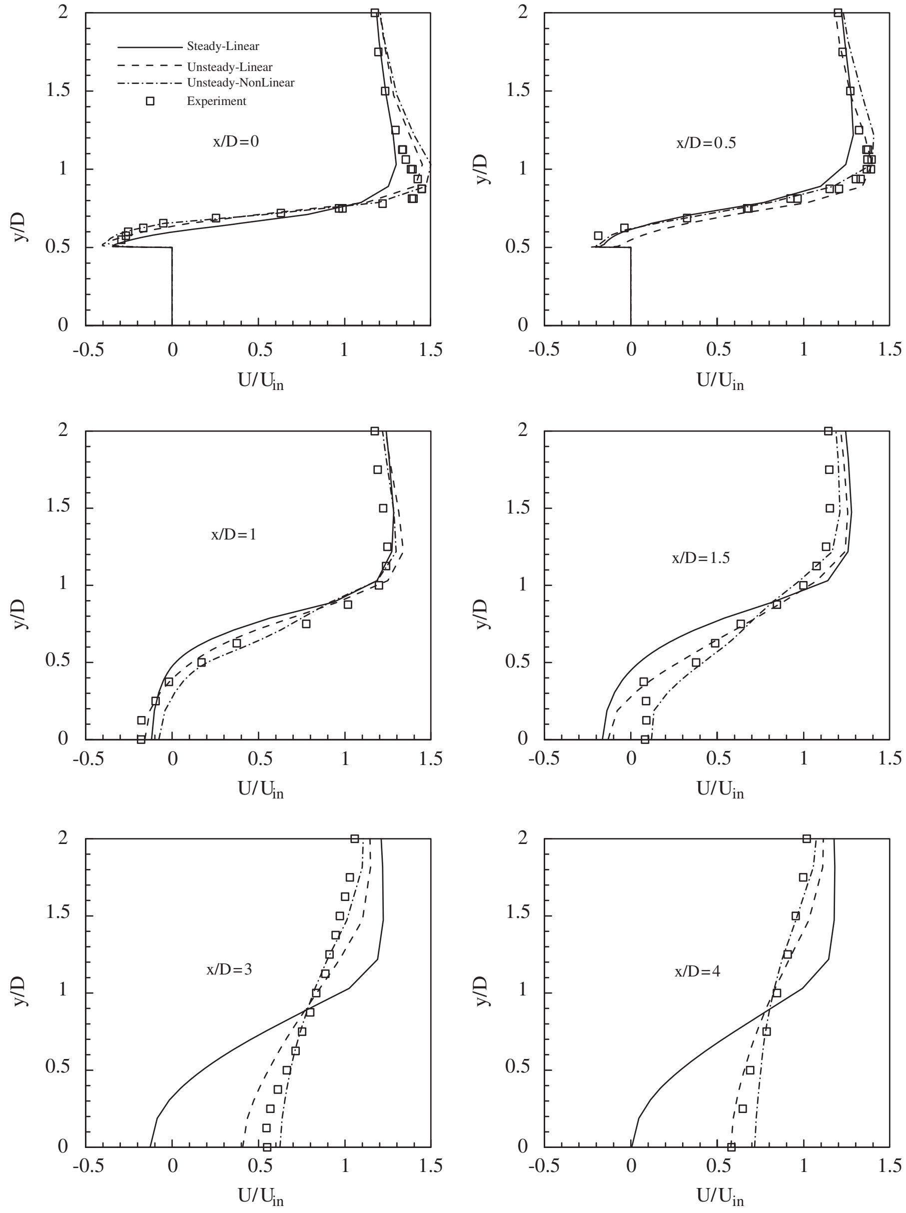

Figure 9. Comparison of predicted stream-wise velocity profiles with experimental data of Lyn *et al.* [7] ($\beta = 7\%$ and $Re = 22000$).

is at its strongest, in agreement with the experimental data, the unsteady flow computations return higher levels of cross-stream velocity than the steady flow ones. Further downstream, $x/D = 3.0$ and 4.0, where the flow oscillations, as shown in Figures 7 and 8, die down, the cross-stream

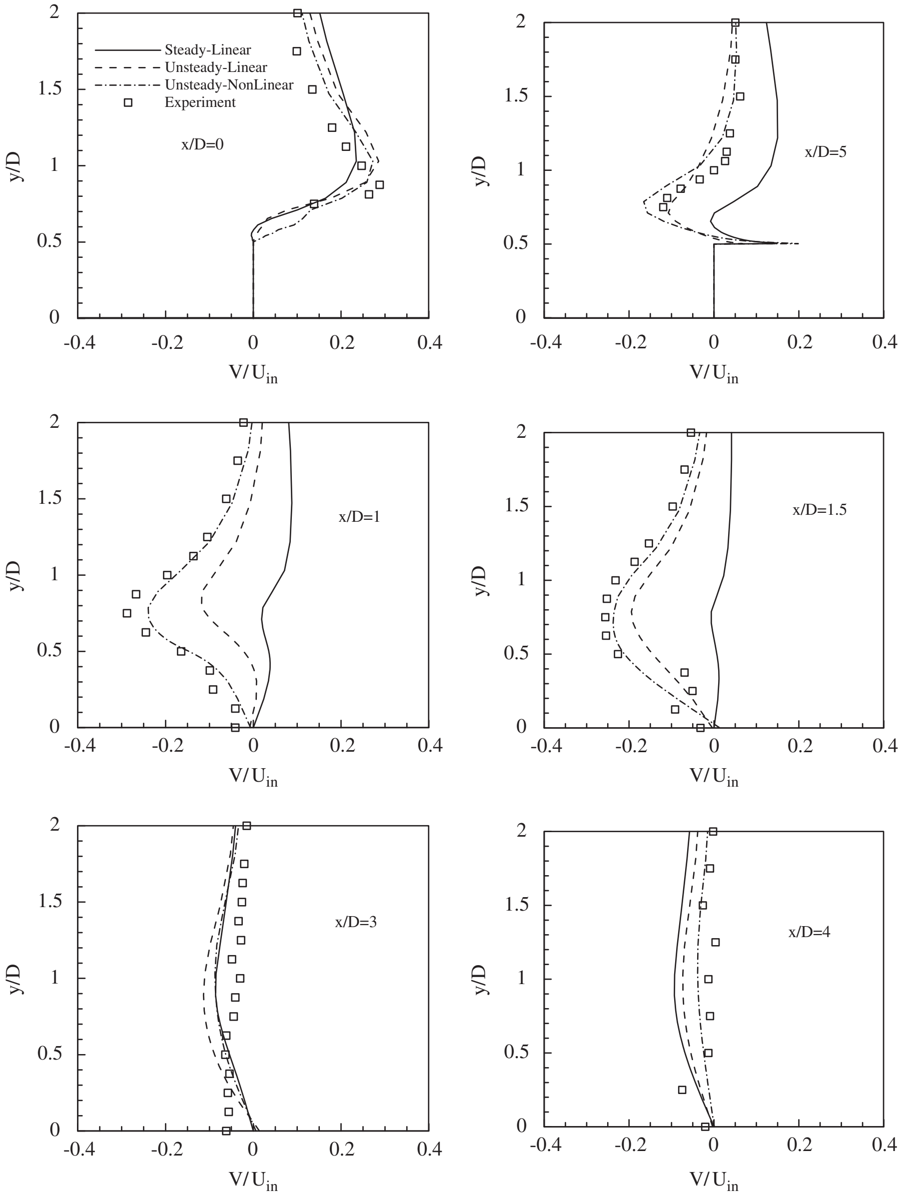

Figure 10. Comparison of predicted cross-stream velocity profiles with experimental data of Lyn *et al.* [7] ($\beta=7\%$ and $Re=22\,000$).

velocity also dies down and the differences between the steady and unsteady predictions decrease. The faster recovery, predicted by the non-linear k–ε, is also consistent with the fact that, as shown in Figure 10, again in closer accord with the measurements, the non-linear model predicts a stronger cross-duct motion within the vortex-shedding region ($x/D=1$ and 1.5).

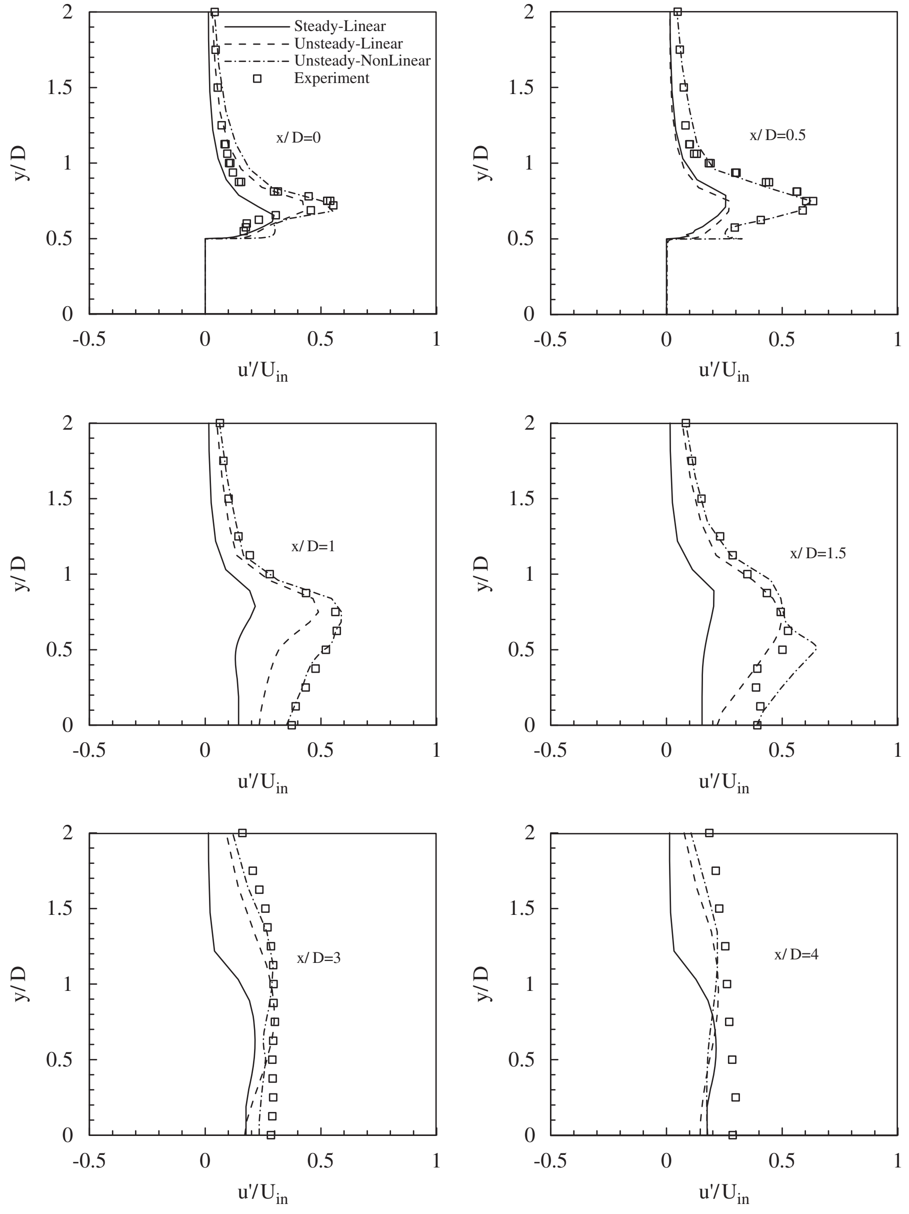

Figure 11. Comparison of predicted stream-wise intensity profiles with experimental data of Lyn *et al.* [7] ($\beta = 7\%$ and $Re = 22\,000$).

Attention is now directed toward the prediction of turbulent quantities. In Figures 11, 12, and 13 the predictions of the steady linear k–ε and unsteady linear and non-linear k–ε models for stream-wise (u'), cross-stream (v') turbulence intensities and turbulent shear stress ($\overline{uv}$), are, respectively

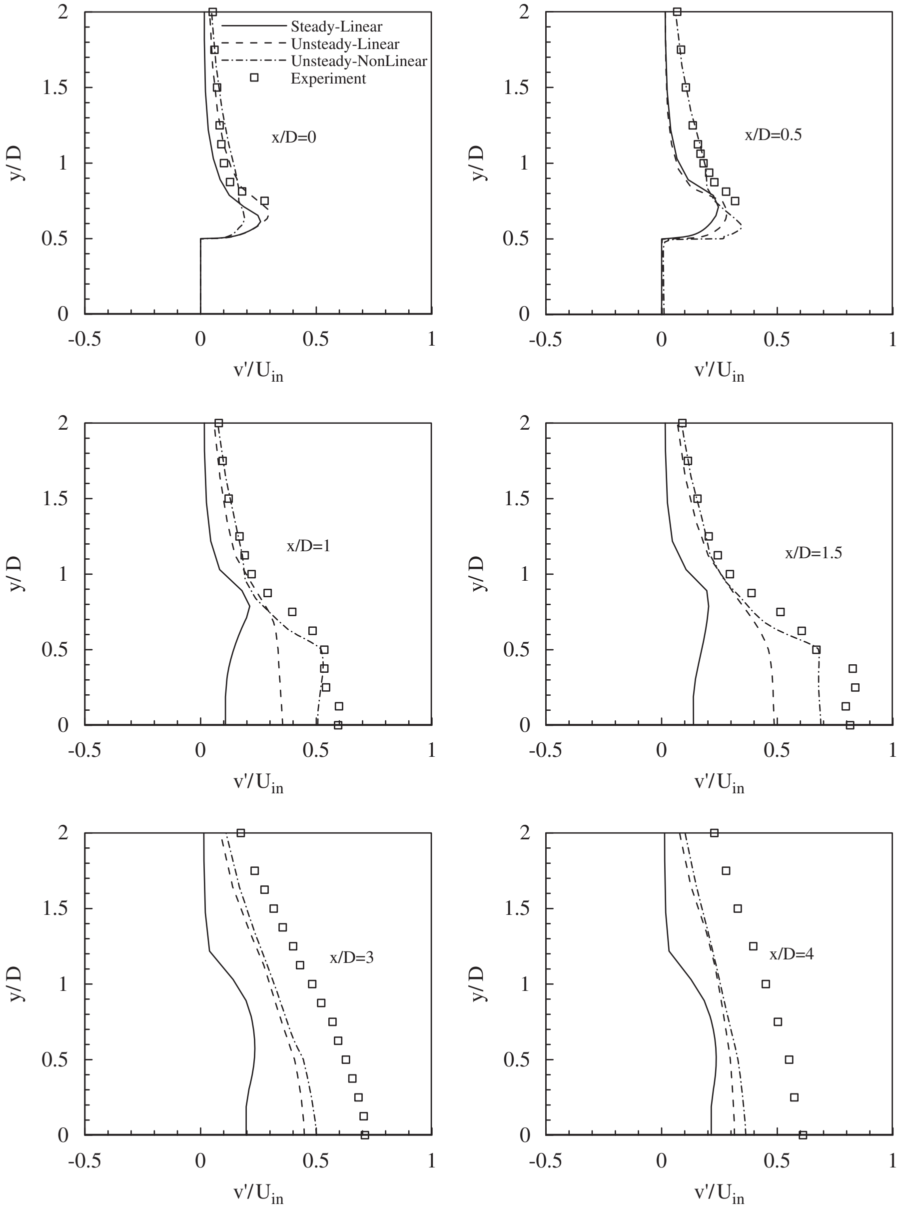

Figure 12. Comparison of predicted cross-stream intensity profiles with experimental data of Lyn *et al.* [7] ($\beta = 7\%$ and $Re = 22\,000$).

shown and compared with measurements of Lyn *et al.* [7]. It should be noted that in the unsteady predictions the total stresses, resolved plus modeled stresses are shown. The resolved stresses are obtained by post-processing the instantaneous velocity field, produced by the ensemble-averaged

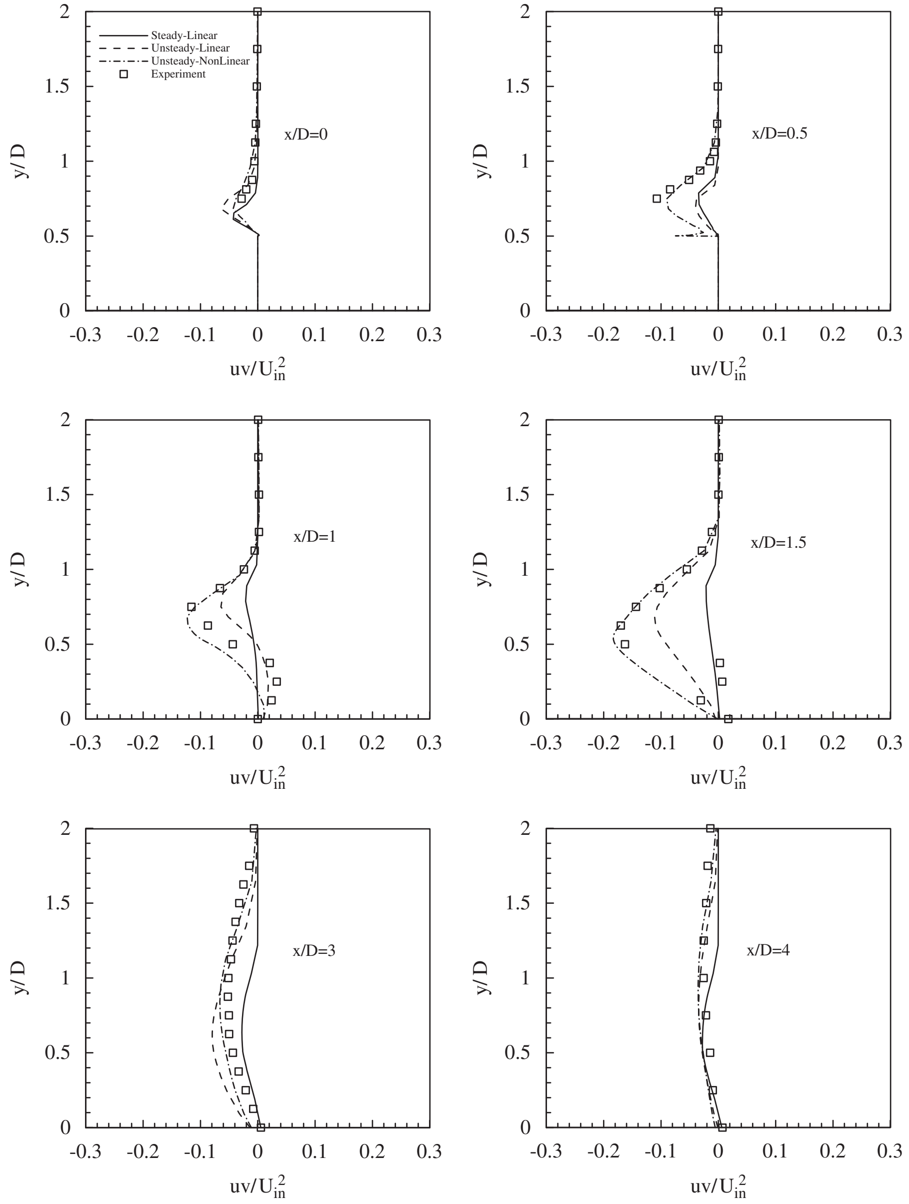

Figure 13. Comparison of predicted turbulent shear stress profiles with experimental data of Lyn *et al.* [7] ($\beta=7\%$ and $Re=22\,000$).

mean flow equations, over a cycle. The modeled stresses are calculated by time averaging the instantaneous Reynolds stresses, which result from the solution of the model equations, over a cycle. Consequently, when the resolved component is a significant part of the total, it is possible to predict a non-isotropic turbulence field, even with a linear k–ε model. One interesting feature that can be observed from the experimental results for turbulence intensities is that, over the obstacle, the stream-wise intensity is higher than the cross-stream intensity, while the reverse occurs within the wake region downstream of the obstacle due to the presence of the flow oscillations in the cross-stream direction. Thus, the flow under investigation demonstrates significant turbulence anisotropy. It is clear that the three measured components of the Reynolds stress tensor (especially the cross-stream component) are seriously under predicted by the steady flow simulations. The unsteady flow predictions of the three measured Reynolds stresses, on the other hand, probably due to the additional contribution of the resolved components, are substantially closer to the data than the corresponding steady flow profiles. Nevertheless, significant discrepancies between the predicted by using unsteady linear k–ε model and measured still remain, especially for the cross-stream intensity. Thus, it appears that, similar to what is observed in the mean velocity comparisons, the unsteady solution of the governing equations does also lead to improvements in prediction of turbulence quantities.

These findings are in line with those of earlier studies, discussed in Section 1, which will suggest that the remaining differences seen between the predictions and measurements, especially in the case of turbulence quantities, must be due to weaknesses of the turbulence model in general and in particular the effective viscosity approximation.

While the linear k–ε model, even in unsteady computations, still under estimates the turbulence quantities, the non-linear k–ε model produces higher turbulence intensities and turbulent shear stress levels, which are also very close to the measured levels. The improvements in the predictions are especially evident in Figure 13, where at all locations (especially within the wake at $x/D=1.0$ and 1.5) introduction of the non-linear k–ε model results in very close agreement between predicted and measured turbulent shear stresses.

The predicted distributions of the time-averaged stream-wise velocity along the center-line of the channel, using the linear and non-linear k–ε models, are compared with the measurements of Lyn *et al.* [7] in Figure 14(a). The U-velocity distribution predicted by the steady flow computations and the linear k–ε model is also included for baseline comparisons. From this figure several features can be observed. In comparison with the experimental data, the steady flow computations with the linear k–ε model produce a substantially longer re-circulation region behind the block, followed by a significantly slower recovery. This is of course consistent with the earlier comparisons. Also consistent with the earlier comparisons is the fact that, in closer accord with the data, the unsteady flow computations return a shorter recirculation length and a faster recovery and that the unsteady flow, non-linear model computations are in very close agreement with the data. The most serious discrepancy between the unsteady predictions and measurements occurs at the downstream of the recovery zone (i.e. $x/D>3.5$), where both turbulence models (especially the non-linear k–ε model) over predict the measured values. As mentioned in the introduction, the flow considered here has been also studied by Rodi [20] using several turbulence modeling approaches. In Figure 14(b), predicted stream-wise velocity along centerline using the non-linear k–ε model is compared with those reported by Rodi [20] using LES, two layer Kato Launder (TL–KL) k–ε model and the Kato Launder k–ε model with wall functions (KL k–ε WF). As before practically all the differences among the predictions occur downstream of the obstacle. The Kato–Launder model with wall functions predicts a downstream separation bubble, which is about twice as long as the measured one, while the two-layer version of the Kato–Launder predicts the correct length of the separation bubble, but a wake recovery which is faster than that of the experimental data. The LES prediction of the centerline variation of the mean velocity shows a stronger backflow than that measured close to the downstream surface of the block, but further downstream they show the correct length

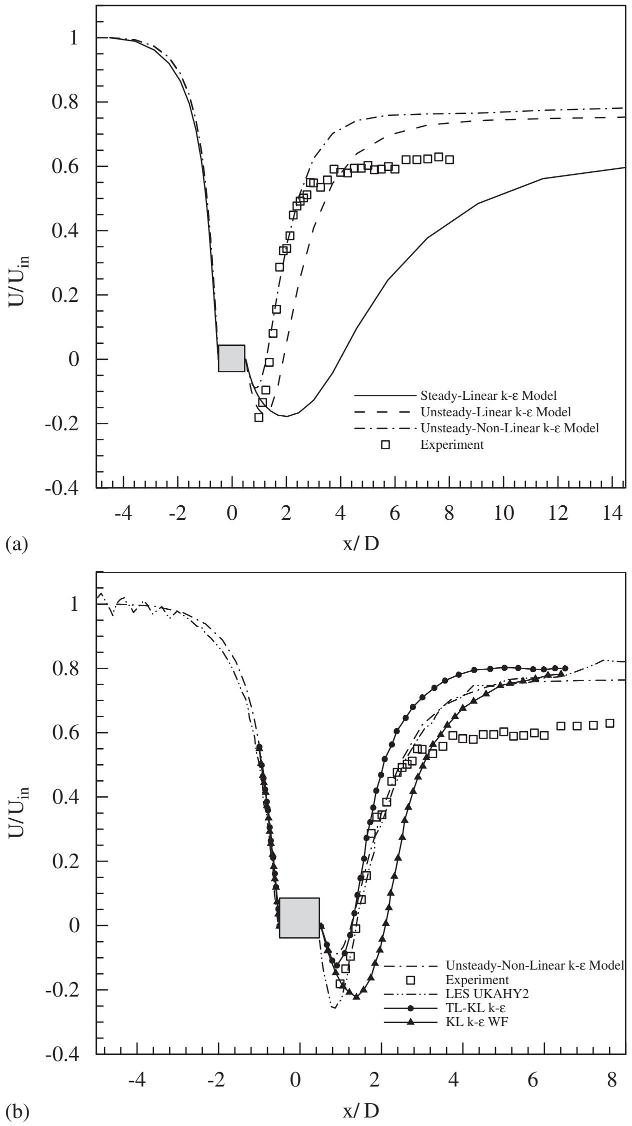

Figure 14. Comparison between the predicted stream-wise velocity with experimental data of Lyn *et al.* [7], LES and KL k–ε results [20] along the horizontal center-line of the channel ($\beta = 7\%$ and $Re = 2.2 \times 10^4$).

of the separation bubble and wake recovery. A little surprisingly perhaps, the non-linear model of the present study returns a mean flow evolution that is closer to the measured development than even that predicted by the LES approach.

In Table III, the recirculation lengths predicted by computations of the current study are compared with those of Rodi [20] and with the measured value of Lyn *et al.* [7]. The unsteady predictions of the recirculation length by the Launder–Sharma k–ε model and the Kato–Launder k–ε model with

Table III. Comparison of recirculation length predicted with turbulence models.

	x_r/D
Exp. (Lyn *et al.* [7])	1.37
Unsteady linear model	2.3
Unsteady non-linear model	1.25
Steady linear model	4.04
LES UKAHY2	1.38
TL–KL k–ε	1.27
KL k–ε WF	2.1

wall functions are close to each other and both models overestimate the length of recirculation bubble. On the other hand, the unsteady predictions of the non-linear k–ε model and the two-layer Kato–Launder k–ε model are more accurate and both are lower than the measured value. Among the predictions presented in Table III, as expected, the worst prediction of recirculation length is returned by the steady computations with the linear k–ε model, while the best result is returned by the LES of Rodi [20].

In Figure 15(a), the predicted distributions of the time-averaged total turbulent kinetic energy along the symmetry plane of the channel, resulting from unsteady computations with the linear and non-linear k–ε models, are compared with measurements of Lyn *et al.* [7]. The k distribution predicted from the steady computations and the linear k–ε model is also included for comparison.

Experimental results reveal that the turbulent kinetic energy rises from zero to its peak value within the wake and then slowly decreases with the development of the flow in the stream-wise direction. It can be observed that both the steady and unsteady computations capture the trend in the k distribution. However, consistent with the results shown in Figures 11 and 12, the centerline levels of turbulence of the steady flow computations of the linear k–ε are well below the measured values. The unsteady flow computations, using the linear k–ε model, return substantially higher k levels. The overall shape of the k distribution is better predicted, but just behind the block, peak levels are still under predicted by about 50%. Introduction of the non-linear model to the unsteady flow computations further increases the predicted turbulence levels within the wake region. Moreover, the location of the peak value of k as well as the overall distribution is now in excellent agreement with the measurements.

In Figure 15(b), corresponding comparisons between the predictions of the non-linear model of the present study with those reported by Rodi [20] are presented. Both versions of the Kato–Launder model over predict the centerline k levels over most of the region downstream of the block. The wall-function version predicts a more gradual rise of centerline k after the block with the peak value further downstream than measured peak level, while the two-layer version predicts the correct location at which k reaches its peak value, but over predicts the k level at the peak location and also over the region downstream of it. The LES predicted k variation, while closer to the data than the two Kato–Launder model predictions show two major deficiencies. The peak level is higher than that measured and closer to the block and while in the initial recovery region ($2<x/D<3$) the k levels are well predicted, further downstream ($x/D>3$) the predicted levels do not fall as rapidly with downstream distance as the measured ones. As was also noted in the

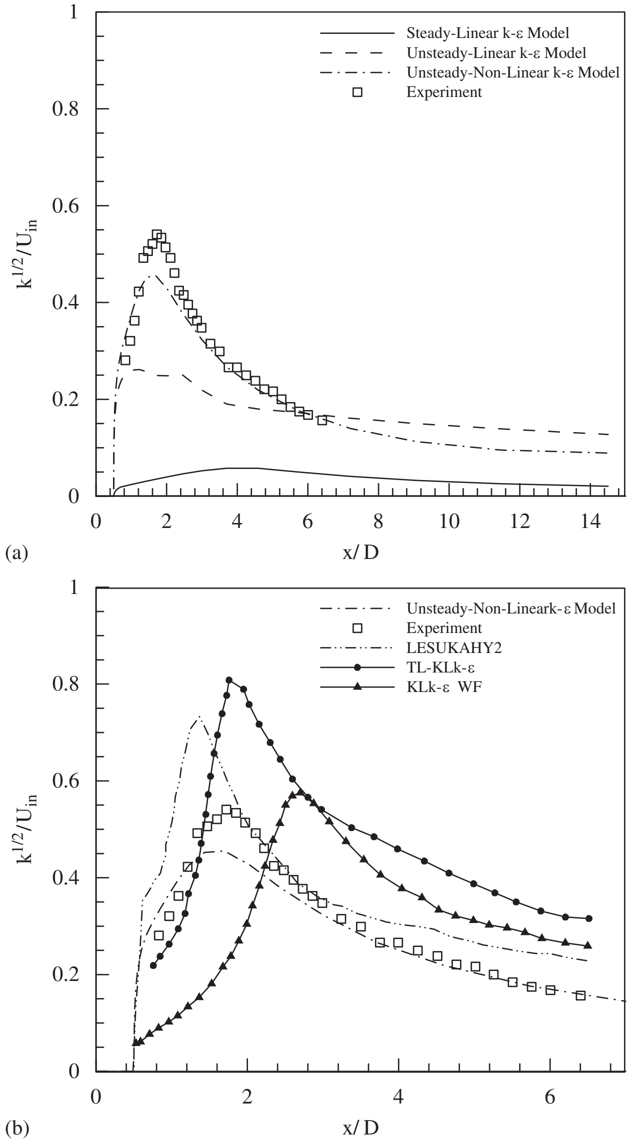

Figure 15. Comparison between the predicted turbulent kinetic energy with experimental data of Lyn *et al.* [7], LES and KL k–ε results [20] along the horizontal center-line of the channel ($\beta = 7\%$ and $Re = 2.2 \times 10^4$).

corresponding mean velocity comparisons of Figure 14(b), the centerline k variation returned by the non-linear k–ε model is closer to the measured variation than even that of the LES approach.

The comparisons of Figures 10–15 suggest that the non-linear k–ε, when used in the 2-D URANS computations of flows around square cylinders, return higher turbulence levels and also a stronger cross-stream motion downstream of the block than the linear model. This in turn results in a faster

Table IV. Comparison of Strouhal number and drag coefficient predicted with turbulence models.

	St	C_D
Exp. (Lyn *et al.* [7])	0.132	2.1
Unsteady linear model	0.115	1.99
Unsteady non-linear model	0.126	2.12
Steady linear model	—	0.16
Steady non-linear model	—	0.19

flow recovery in the downstream region. The flow behavior predicted by the non-linear k–ε within the 2-D URANS framework is in close accord with the measured time-averaged motion. Indeed comparison with earlier attempts shows that the non-linear two-dimensional URANS predictions of the time-averaged flow are as close to the measurements as earlier LES predictions and superior to those of other URANS computations. This close agreement suggests that on the one hand the large-scale unsteady motion that results from a flow around a cylinder is mainly two-dimensional, and on the other hand that it can only be successfully predicted (with URANS) with turbulence models that take into account the anisotropy of turbulence.

From the practical point of view, two of the most important parameters for engineering applications of unsteady flow around bluff bodies are the Strouhal number and drag coefficient. The predicted values for these parameters, using turbulence models used in this work, are compared with experimental data of Lyn *et al.* [7] in Table IV. Starting with the drag coefficients obtained from the steady solutions, as expected, these are substantially lower, less than 10%, than the value of the measured drag coefficient. These large disparities between the steady-state predictions and the measurement suggest that the vortex shedding behind the obstacle makes the largest contribution to the drag coefficient. Therefore, many studies have focussed on the ways to control and suppress the vortex shedding in the positions where great value of drag force is unfavorable. The 2-D URANS comparisons show that the predicted values for both the Strouhal number and the drag coefficient, using the two turbulence models, are close to the measured values. For the unsteady flow linear model computations, the predicted Strouhal number is 12.8% lower than that of the experiments and the drag coefficient is 5.2% lower. The corresponding figures for the unsteady flow non-linear model computations are 4.5% lower and 1% higher, respectively, providing further evidence of the superiority of the non-linear model. The uncertainty value for Strouhal number in the experimental results is quoted as 3%.

Finally for the non-linear model, Figures 16, 17, and 18 demonstrate the separate contributions of the resolved and modeled components of Reynolds stresses to the total stress, which is also compared with the experimental data. As can be noted, the resolved component makes an important contribution to the total level, not only for the normal stresses, but also for the turbulent shear stress. The latter is an indication that the unsteady motion enhances the mixing of momentum and explains why it is necessary to employ URANS for the computation of such flows.

8. CONCLUSIONS

In this paper two low-Reynolds number k–ε models have been employed to compute unsteady turbulent flow around a square cylinder confined in a channel. The results presented show that,

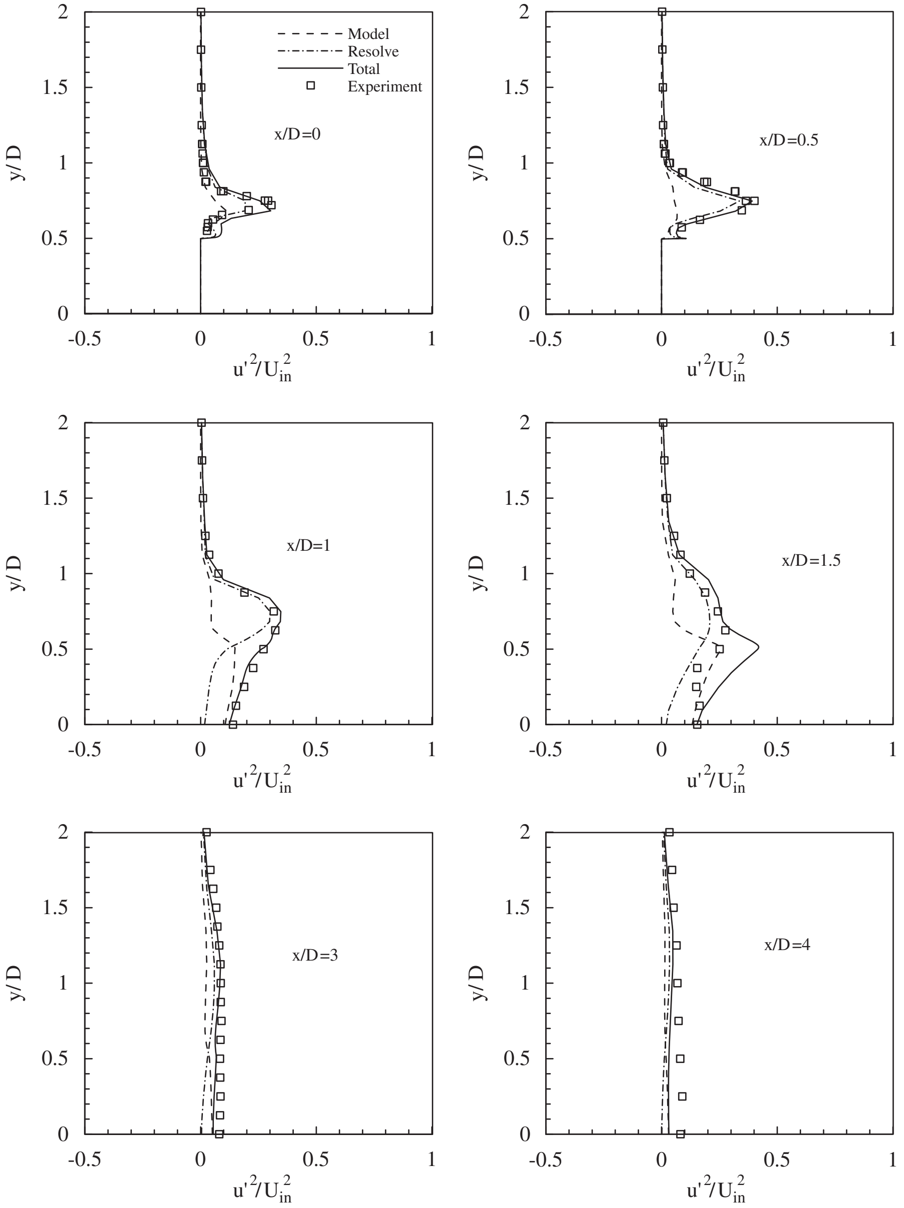

Figure 16. Contributions of the modeled and resolved components to the total stream-wise normal Reynolds stress.

as expected, the steady solution of governing equations does not produce accurate predictions of the time-averaged flow and it becomes necessary to perform unsteady 2-D calculations for more reliable predictions of these flows. This suggests that large-scale unsteady flow structures make a significant contribution to the mixing of momentum.

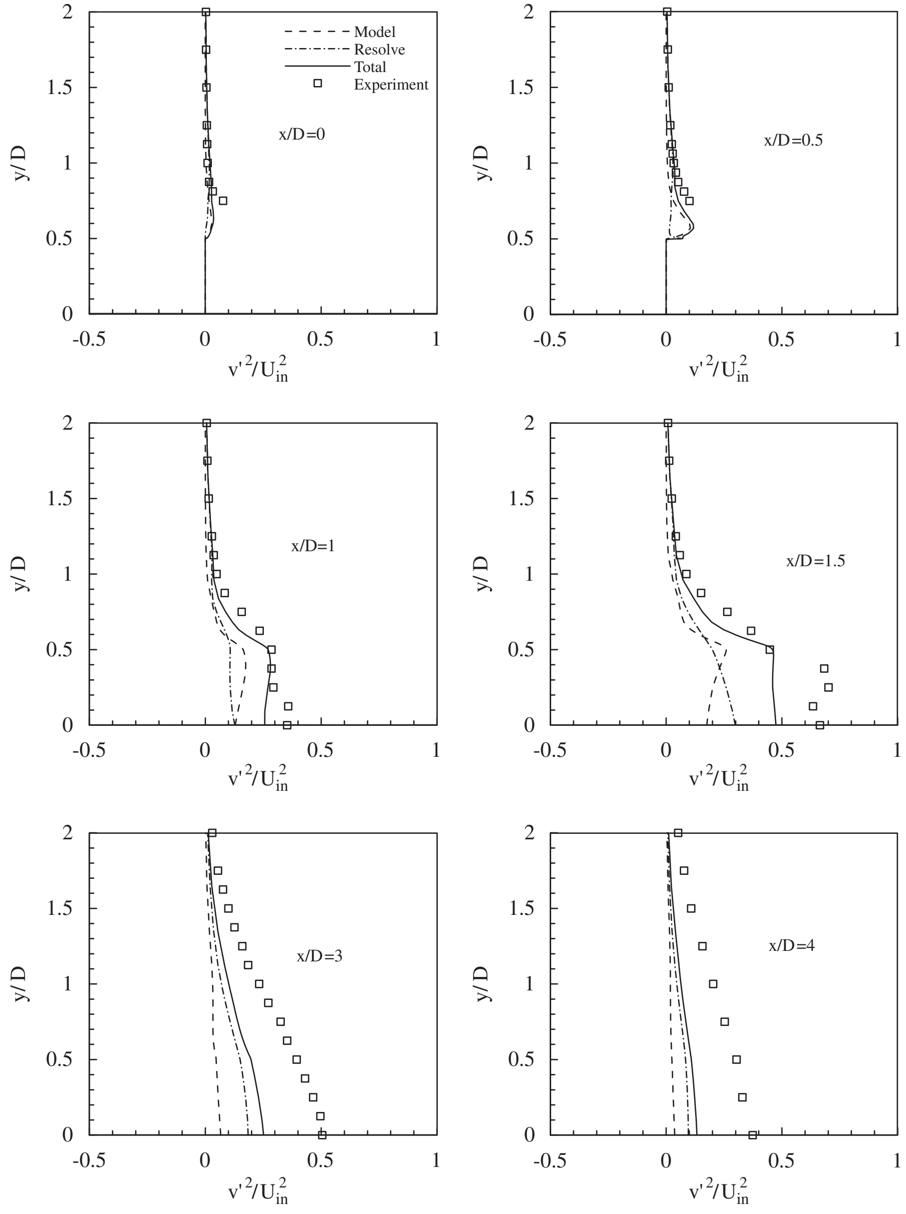

Figure 17. Contributions of the modeled and resolved components to the total cross-stream turbulent normal stress.

Use of the 2-D URANS approach, as also found in earlier studies, leads to a significant improvement in the predictions of the time-averaged flow and turbulence fields and also of global parameters such as the drag coefficient and the Strouhal number.

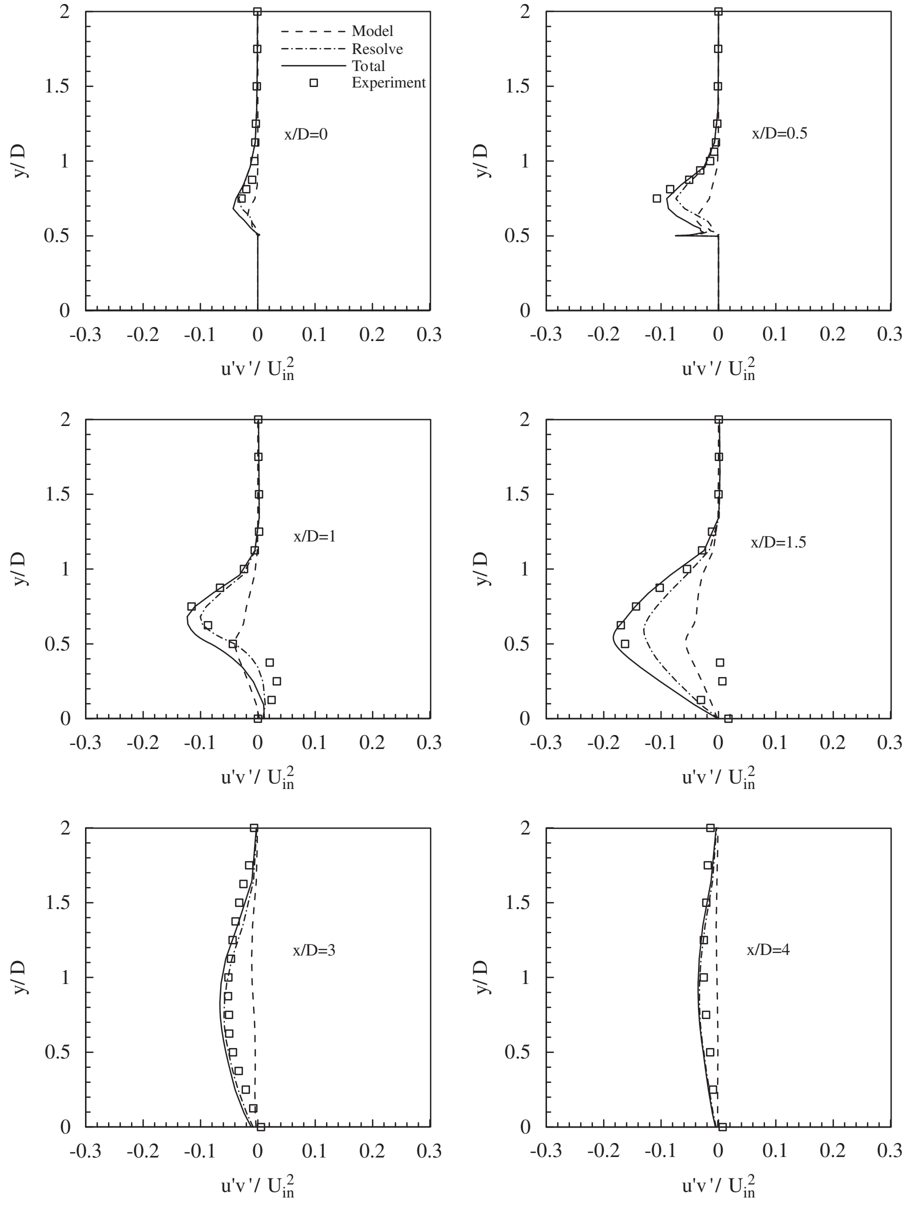

Figure 18. Contributions of the modeled and resolved components to the total turbulent shear stress.

Even within the 2-D URANS strategy, however, the low-*Re* linear *k*–ε model tested, showed predictive deficiencies, such as a slow mean flow recovery downstream of the obstacle, under-predicted cross-stream mean motion, and also under-predicted turbulent stresses in the wake region. Introduction of the Craft *et al.* [22] non-linear version of the low-*Re* *k*–ε model brought the time-averaged 2-D URANS computations to close agreement with corresponding local and global measurements. This suggests that the large-scale flapping motion behind the square cylinder is mainly two dimensional and also that the flow evolution is strongly influenced by the anisotropy of the turbulence field. The latter makes it necessary to use turbulence models that account for the effects of turbulence anisotropy. Consequently, further work must also explore the use of second-moment closures.

REFERENCES

1. Lee BE. The effect of turbulence on the surface pressure field of a square prism. *Journal of Fluid Mechanics* 1975; **69**:263–282.
2. Knisely CW. Strouhal number of rectangular cylinder at incidence: a review and new data. *Journal of Fluids and Structures* 1990; **4**:371–393.
3. Norberg C. Flow around rectangular cylinders: pressure forces and wake frequencies. *Journal of Wind Engineering and Industrial Aerodynamics* 1993; **49**:187–196.
4. Bearman PW, Trueman DM. An investigation of the flow around rectangular cylinder. *Aeronautical Quarterly* 1972; **23**:229–237.
5. Okajima A, Nagashisa T, Rokugoh A. A numerical analysis of flow around rectangular cylinders. *JSME International Journal*, *Series II* 1990; **33**:702–711.
6. Lyn DA, Rodi W. The flapping shear layer formed by flow separation from the forward corner of a square cylinder. *Journal of Fluid Mechanics* 1994; **267**:353–376.
7. Lyn DA, Einva S, Rodi W, Park JH. A laser-doppler velocimetry study of ensemble averaged characteristics of the turbulent near wake of a square cylinder. *Journal of Fluid Mechanics* 1995; **304**:285–319.
8. Fromm JE, Harlow FH. Numerical solution of the problem of vortex street development. *Physics of Fluids* 1963; **6**:975–982.
9. Davis RW, Moor EF, Purtell LP. A numerical experimental study of confined flow around rectangular cylinders. *Physics of Fluids* 1984; **27**:40–59.
10. Tamura T, Kuwahara K. Numerical study of aerodynamics behavior of a square cylinder. *Journal of Wind Engineering and Industrial Aerodynamics* 1990; **33**:161–170.
11. Kawamura H, Kawashima N. An application of a near-wall k–$\tilde{\varepsilon}$ model to the turbulent channel flow with transpiration and to the oscillatory flow around a square cylinder. *Second International Symposium on Turbulence*, *Heat and Mass Transfer*, Delft University, 1997; 379–388.
12. Sohankar A, Davidson L, Norberg C. Numerical simulation of unsteady flow around a square two-dimensional cylinder. *Twelfth Australasian Fluid Mechanics Conference*, University of Sydney, Australia, 1995; 517–520.
13. Richmond-Bryant J. Verification testing in computational fluid dynamics: an example using Reynolds-averaged Navier–Stokes methods for two-dimensional flow in the near wake of a circular cylinder. *International Journal for Numerical Methods in Fluids* 2003; **43**:1371–1389.
14. Boussinesq J. Theories de Lecoulment Tourbillant. *Mem. Pres. Par Div. Savant a Local Sciences*, Paris, 1877; 23–46.
15. Craft TJ, Launder BE, Suga K. Development and application of a cubic eddy-viscosity model of turbulence. *International Journal of Heat and Fluid Flow* 1996; **17**:108–115.
16. Bocsh G, Rodi W. Simulation of vortex shedding past a square cylinder with different turbulent models. *International Journal for Numerical Methods in Fluids* 1998; **28**:601–616.
17. Kato M, Launder BE. The modeling of turbulent flow around stationary and vibrating square cylinders. *Proceedings of the 9th Symposium on Turbulent Shear Flows*, Kyoto, 1993; 10–14.
18. Younis BA, Przulj VP. Computation of turbulent vortex shedding. *Computational Mechanics* 2006; **37**:408–425.
19. Saha AK, Biswas G, Muralidhar K. Numerical study of turbulent unsteady wake behind a partially enclosed square cylinder using RANS. *Computer Methods in Applied Mechanics and Engineering* 1999; **178**:323–341.
20. Rodi W. Comparison of LES and RANS calculations of the flow around bluff bodies. *Journal of Wind Engineering and Industrial Aerodynamics* 1997; **69–71**:55–75.
21. Launder BE, Sharma BL. Application of the energy dissipation model of turbulence to the calculation of flow near a spinning disc. *Letter in Heat Mass Transfer* 1974; **1**:131–138.

22. Craft TJ, Launder BE, Suga K. Extending the applicability of eddy viscosity models through the use of deformation invariants and non-linear elements. *Proceedings of the 5th International Symposium on Refine Flow Modeling and Turbulence Measurements*, Paris, 1993; 125–132.
23. Raisee M, Alemi H, Iacovides H. Prediction of developing turbulent flow in 90°-curved ducts using linear and non-linear low-*Re* k–ε models. *International Journal of Numerical Methods for Heat and Fluid Flow* 2006; **51**:1379–1405.
24. Raisee M, Noursadeghi A, Iacovides H. Application of a non-linear k–ε model in prediction of convective heat transfer through ribbed passages. *International Journal of Numerical Methods for Heat and Fluid Flow* 2004; **14**(3):285–304.
25. Craft TJ, Iacovides H, Momeni P. Modelling the effect of forced unsteadiness on flow and heat transfer in separated and reattaching flows TSFP7. *Seventh International Symposium on Turbulence and Shear Flow Phenomena*, Munich, August 2007.
26. Jones WP, Launder BE. The prediction of laminarization with a two equation model of turbulence. *International Journal of Heat and Mass Transfer* 1972; **15**:301–314.
27. Craft TJ, Iacovides H, Yoon JH. Progress in the use of non-linear two-equation models in the computation of convective heat transfer in impinging and separated flows. *Turbulence Flow and Combustion* 1999; **63**:59–80.
28. Yap CR. Turbulent heat transfer and momentum transfer in reticulating and impinging flow. *Ph.D. Thesis*, Faculty of Technology, University of Manchester, U.K., 1987.
29. Iacovides H, Raisee M. Computation of flow and heat transfer in two-dimensional rib-roughened passages, using low-Reynolds-number turbulence models. *International Journal of Numerical Methods for Heat and Fluid Flow* 2001; **11**(2):138–155.
30. Durbin PA. Near-wall turbulence closure modeling without damping function. *Theoretical and Computational Fluid Dynamics* 1991; **3**:1–13.
31. Rhie CM, Chow WL. Numerical study of the turbulent flow past an airfoil with trailing edge separation. *AIAA Journal* 1983; **21**:1525–1532.
32. Iacovides H. The computation of turbulent flow through stationary and rotating U-bends of with rib-roughened surfaces. *Proceedings of the 11th International Conference on Laminar and Turbulent Flows*, Swansea, U.K., 1997.
33. Crank J, Nicolson P. A practical method for numerical evaluation of solutions for partial differential equations of the heat conduction. *Proceedings of the Cambridge Philological Society* 1974; **43**:50–67.

DOI: 10.1002/fld